

See discussions, stats, and author profiles for this publication at: <https://www.researchgate.net/publication/324301702>

# Application of supervised machine learning for defect detection during metallic powder bed fusion additive manufacturing using high resolution imaging

Article · April 2018

DOI: 10.1016/j.addma.2018.04.005

---

CITATIONS

9

5 authors, including:



E.W. Reutzel  
Pennsylvania State University

83 PUBLICATIONS 539 CITATIONS

[SEE PROFILE](#)

READS

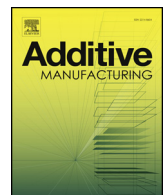
228



S. Phoha  
Pennsylvania State University

152 PUBLICATIONS 1,102 CITATIONS

[SEE PROFILE](#)



## Full Length Article

# Application of supervised machine learning for defect detection during metallic powder bed fusion additive manufacturing using high resolution imaging.

Christian Gobert<sup>a</sup>, Edward W. Reutzel<sup>b,\*</sup>, Jan Petrich<sup>c</sup>, Abdalla R. Nassar<sup>b</sup>, Shashi Phoha<sup>c</sup><sup>a</sup> Department of Mechanical Engineering, Pennsylvania State University, State College, PA 16804-0030, United States<sup>b</sup> Applied Research Laboratory, Pennsylvania State University, P.O. Box 30, Mail Stop 4420D, State College, PA 16804-0030, United States<sup>c</sup> Applied Research Laboratory, Pennsylvania State University, P.O. Box 30, Mail Stop 5700D, State College, PA 16804-0030, United States

## ARTICLE INFO

**Keywords:**  
 Additive manufacturing  
 Powder bed fusion  
 Process monitoring  
 Machine learning  
 Experimental validation

## ABSTRACT

Process monitoring in additive manufacturing (AM) is a crucial component in the mission of broadening AM industrialization. However, conventional part evaluation and qualification techniques, such as computed tomography (CT), can only be utilized after the build is complete, and thus eliminate any potential to correct defects *during* the build process. In contrast to post-build CT, *in situ* defect detection based on *in situ* sensing, such as layerwise visual inspection, enables the potential for *in-process* re-melting and correction of detected defects and thus facilitates *in-process* part qualification. This paper describes the development and implementation of such an *in situ* defect detection strategy for powder bed fusion (PBF) AM using supervised machine learning.

During the build process, multiple images were collected at each build layer using a high resolution digital single-lens reflex (DSLR) camera. For each neighborhood in the resulting layerwise image stack, multi-dimensional visual features were extracted and evaluated using binary classification techniques, i.e. a linear support vector machine (SVM). Through binary classification, neighborhoods are then categorized as either a flaw, i.e. an undesirable interruption in the typical structure of the material, or a nominal build condition. Ground truth labels, i.e. the *true* location of flaws and nominal build areas, which are needed to train the binary classifiers, were obtained from post-build high-resolution 3D CT scan data. In CT scans, discontinuities, e.g. incomplete fusion, porosity, cracks, or inclusions, were identified using automated analysis tools or manual inspection. The xyz locations of the CT data were transferred into the layerwise image domain using an affine transformation, which was estimated using reference points embedded in the part. After the classifier had been properly trained, *in situ* defect detection accuracies greater than 80% were demonstrated during cross-validation experiments.

## 1. Introduction

Metallic additive manufacturing (AM) is a process in which near-net-shape parts are built in a layer-by-layer manner from powder alloys directly from digital files. Powder bed fusion AM (PBFAM) is a form of AM in which a laser selectively melts consecutive layers of metal powder placed on a build platform inside a build chamber [1]. After each melt cycle, a new layer of metal powder is spread across the build platform by a recoater blade, rake, or roller. PBFAM parts are made up of hundreds or thousands of layers (typically ~20–60 µm layer thickness) dependent on part dimensions and material; and build times range from hours to days [2]. However, discontinuities in PBFAM parts—e.g. incomplete fusion, porosity, cracks, or inclusions—may arise from

contamination or irregularities in powder recoating, laser-material interaction, or part solidification [3], and are thus a common concern, negatively affecting mechanical properties [4–6].

Detection and/or mitigation of such discontinuities may, however, be possible through monitoring of the AM build process. Indeed, research on process monitoring of AM systems has increased in the past decade, driven by AM's appeal for manufacturing of complex high-value and low-volume production parts [7]. A common approach to process monitoring is measurement of melt pool characteristics. Melt-pool monitoring can provide insight into part quality and process phenomena, however melt-pool monitoring systems require tight integration with high speed scanners, and analysis can be complicated due to challenges when calibrating the emissivity of the melt pool [7].

\* Corresponding author.

E-mail addresses: Cyg5184@arl.psu.edu (C. Gobert), Ewr101@arl.psu.edu (E.W. Reutzel), Jup37@arl.psu.edu (J. Petrich), Arn5000@arl.psu.edu (A.R. Nassar), Sxp26@arl.psu.edu (S. Phoha).

Alternatively, imaging of build layers before or after a laser exposure offers an inexpensive and system-independent approach for defect detection compared to melt-pool metrology and post-evaluation techniques [8]. Here, this strategy is termed layerwise imaging.

Layerwise process monitoring has been attempted using visible-light and infrared (IR) imaging. Kleszczynski et al. [9] presented a system-independent layerwise-imaging system, with a 29-megapixel charge-coupled device (CCD) camera, which captured process irregularities on in situ surfaces of PBFAM parts. Jacobsmühlen et al. [10] expands on Kleszczynski et al. by building a connection between the detection of these surface irregularities and mechanical part performance. Mireles et al. [11] presented a low-resolution IR-layerwise imaging system on a PBFAM process to observe seeded void discontinuities in parts. Geometries of porous discontinuities were measured with contour tracing in the IR-layerwise and CT images. A formal comparison revealed that a substantial difference of measured geometry existed between the two domains. Schwerdtfeger et al. [12] demonstrated a correspondence between low-resolution IR-layerwise imaging and metallographic imaging of electron-beam-based PBFAM parts.

Despite the promise of layerwise monitoring, post-process inspection is still the de facto method for defect detection in AM parts. Spierings et al. [13] compared and contrasted techniques for post-process porosity analysis of PBF parts, including Archimedes methods, metallographic imaging and CT scanning. They note that successful void detection in CT images, relative to Archimedes method, is subject to the selected size threshold for detection of voids, i.e. a larger threshold will prevent detection of smaller voids. In [14] Wits et al. demonstrated that inspection of AM parts using Archimedes, microscopic and CT methods predict similar porosities, however CT scanning enables part porosity to be quantified.

Two strategies can be used to improve conclusions drawn from layerwise data: fusion of multiple layerwise image sets, or fusion of layerwise images with a separate data stream. Information fusion between layerwise images from homogeneous sensors, defined as similar sensors under different conditions that form a complimentary sensor configuration, provides a higher confidence in the interpretation of an observation. Fusing CT data and layerwise images forms a cooperative sensor configuration built from heterogeneous sensors, non-alike sensors, thereby deriving information that cannot be observed by the sensors individually [15]. Weckenmann et al. [15] illustrated that the use of multisensory data fusion, as compared to single sensor applications, reduces uncertainty in dimensional metrology, and provides a more complete description. Aminzadeh and Kurfess [16] proposed the detection of defects in PBF parts using online visual inspection sensors, in varying sensor configuration, paired with classifiers, potentially neural networks or support vector machines (SVMs), but their proposed strategy was not demonstrated.

Supervised machine learning is generally executed in two steps. First, the system is trained, implying that the parameters of the underlying classification scheme are estimated using a training data set with known labels, i.e. the ground truth. For SVM classification, training entails the construction of a decision boundary that best separates the given training data points based on ground truth labels [17]. Second, the performance of the trained classification scheme and associated decision boundary is tested by generating predicted labels for a previously unseen data set, i.e. the test data set. A formal comparison between predicted labels and ground truth labels of the test data set then reveals the *out-of-sample* classification performance, which typically includes metrics such as false positive rates and false negative rates. This procedure is commonly referred to as cross-validation.

In this work, a methodology to train an SVM classifier to detect discontinuities from in situ sensor data using labeled ground truth data extracted from post-build CT scans is developed and demonstrated. The overall strategy is illustrated in Fig. 1.

The details of each block in the diagram are detailed in the Section 2. Algorithms for automated acquisition of ground truth labels from CT

scan data (a discontinuity vs. a nominal build condition), and for transfer of these labeled data from the CT scan domain into an in situ sensor domain (in this case, the layerwise image domain) are developed. An approach for 3D feature extraction from the in situ sensor data and the implementation of an ensemble classification scheme for discontinuity detection performed in the in situ sensor domain is also developed and presented.

Section 3 details the implementation of the proposed methodologies on a single PBFAM part, whereby a digital single lens reflex (DSLR) camera, serving as the in situ sensor, captures multiple images for each build layer (both post-powder re-coat and post-laser exposure) under various lighting conditions. A linear SVM ensemble classifier that fuses visual information extracted from these images is trained using ground truth labels acquired from the CT scan of the part. A cross-validation scheme for the ensemble classifier is implemented in order to formally evaluate classification performance on the set of labeled layerwise image data. Section 4 discusses the results, including a description of the discontinuity geometries identified in the AM part, and the classification results for the detection of discontinuities using in situ images. The final section summarizes the results, and outlines future work.

## 2. Methodology

This paper investigates the hypothesis that in situ sensors monitoring a metal PBFAM process, specifically high resolution imaging of build surfaces, can capture features that can be linked to discontinuities or defects in the resultant component. In this work, *discontinuities* are defined as interruptions in the typical or nominal structure of a material [18]. Discontinuities, such as porosity, can be powder-induced or process-induced, and commonly arise as a result of part solidification, from process errors in a nominal build environment, or whenever process parameters deviate too much from their nominal settings [4]. Porosities can be entrapped gas pores, appearing spherical in shape and with diameters in the order of ten of microns, or elongated voids arising from a lack of fusion between powder particles that can extend to several hundred microns in length [19]. Loosely following standard weld terminology, in this work *defects* are defined as discontinuities that could lead to rejection of the component, and that would be candidates for repair.

For this investigation, ground truth regarding the presence, location, size, and morphology of discontinuities is established using an automated anomaly detection methodology for CT scans developed by PSU/ARL. As a result, each three-dimensional (3D) neighborhood was labeled as either anomalous or nominal. Through manual inspection of the CT scan by a skilled operator, anomalous regions were confirmed to represent actual discontinuities in the material. Given the known part geometry and the introduction of unique reference points, the 3D locations of anomalous and nominal neighborhoods were then transferred from the CT scan domain into the in situ sensor domain, i.e. the stack of layerwise images collected throughout the build process. Using the associated labels “anomalous” and “nominal”, supervised machine learning (in this case, a linear SVM) can be employed in order to attempt the detection of discontinuities using only layerwise images of the build surface. The strategy is outlined below, and displayed schematically in Fig. 1.

### 2.1. Acquisition of ground truth labels from CT scan data

In order to properly train the binary SVM classifier, ground truth labels, i.e. the *true* locations of discontinuities and nominal build areas, are needed in the in situ sensor (or layerwise image) domain. Because discontinuities are not immediately obvious to a human observer using only layerwise imagery collected during the build process, ground truth labels and coordinates of true discontinuities had to be extracted from CT scan data. CT scan data provides a high resolution 3D representation of a part, discretized into a defined voxel size  $d_{CT}$  usually on the order

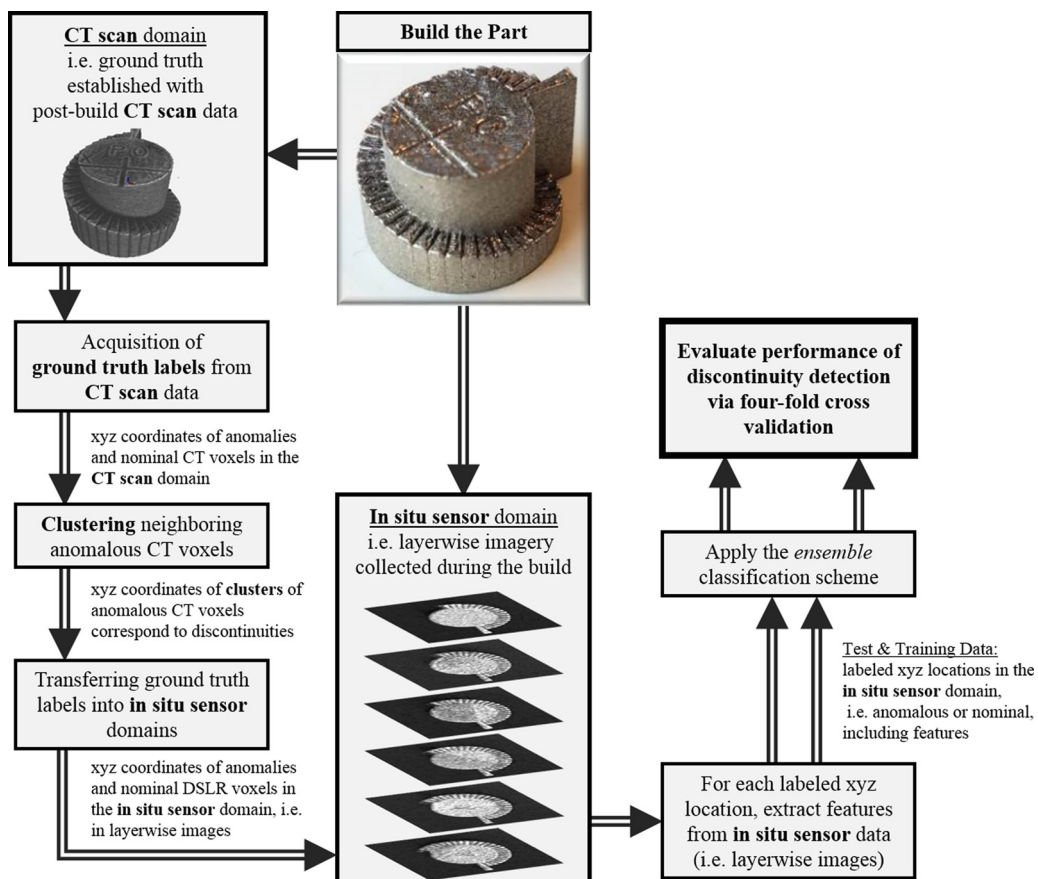


**Fig. 1.** High-level process schematic showing (i) extraction of anomalies from CT scan including transfer of coordinates to the CT scan domain on the left, (ii) in situ sensor imagery at the center, and (iii) feature extraction, supervised machine learning and performance evaluation on the right.

of tens of microns, in which anomaly detection can be accomplished reliably via automated processing or manual inspection. Each CT voxel provides a gray scale intensity value  $I_{CT}$  which represents the local part density as a function of voxel location,  $x_{CT}$ ,  $y_{CT}$ ,  $z_{CT}$ , corresponding to the row, column, and layer, respectively. This can be represented as

$$I_{CT}(x_{CT}, y_{CT}, z_{CT}) \in \mathbb{R} \quad (1)$$

Discontinuities manifest themselves in the CT scan through irregular intensity values as compared to their surroundings. These anomalous CT voxels can be divided into two classes: (i) low-intensity voxels surrounded by higher-intensity voxels (most likely voids resulting from incomplete fusion or entrapped gas porosity), and (ii) high-intensity voxels surrounded by lower-intensity voxels (likely an indicator of contamination or other inclusions). These two cases are clearly evident in the CT scans shown in Fig. 2.

Detection of discontinuities in CT can be automated by analyzing the first and second spatial derivatives over the intensity field, as shown in Eq. (1). Local extrema of  $I_{CT}$  represent anomalous CT voxels which may be linked to actual discontinuities. Using image processing, second derivatives of  $I_{CT}$  are extracted using a 3D convolution operation and a Gaussian kernel of the form

$$G_{3D}(x, y, z, \sigma) = \frac{1}{(\sqrt{2\pi}\sigma)^3} e^{\left(-\frac{x^2+y^2+z^2}{2\sigma^2}\right)} \quad (2)$$

A slice plot of the 3D kernel is shown on the right in Fig. 2. In Eq. (2), the parameter  $\sigma$  is the standard deviation of the underlying Gaussian envelope, and  $x, y, z \in Z$  are the coordinates of the kernel in the 3D CT space with values defined by the domain below

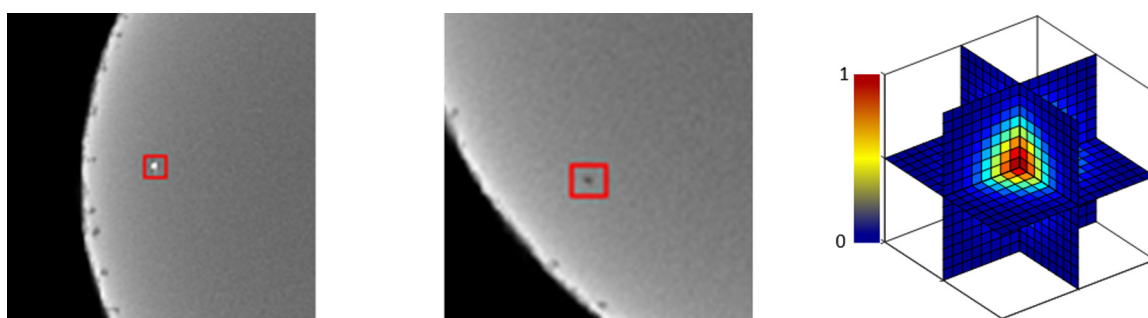


**Fig. 2.** Discontinuities as seen in CT scan showing high-intensity voxels, likely caused by inclusions, surrounded by lower-intensity voxels (left) and low-intensity voxels, most likely voids or pores, surrounded by higher-intensity voxels (center). The 3D Gaussian filter  $G_{3D}$  from (2) used for anomaly extraction in CT is shown on the right.

$$Z = \left\{ -\frac{(S-1)}{2}, \dots, +\frac{(S-1)}{2} \right\} \quad (3)$$

The size of the Gaussian kernel, measured in voxels along each Cartesian axis, is defined by the parameter  $S$  in Eq. (3). Increasing or decreasing  $\sigma$  then allows for the extraction of larger or smaller anomalies in CT, respectively.

The convolution response of the CT scan data, Eq. (1), with respect to the 3D Gaussian kernel, Eq. (2), is obtained using the convolution operator  $*$ , that is

$$F_{CT}(x_{CT}, y_{CT}, z_{CT}) = I_{CT}(x_{CT}, y_{CT}, z_{CT}) * G_{3D} \quad (4)$$

Again, large negative convolution responses may indicate incomplete fusion or porosity, see center plot in Fig. 2, while large positive convolution responses indicate potential inclusions, see left plot in Fig. 2.

In this work, anomalous CT voxels are identified as having convolution responses that fall outside  $g_a$  standard deviations of the mean convolution response of the part. Increasing the value of  $g_a$  increases the severity of the detected anomalies, i.e. their intensity deviation from the mean, but reduces the total number of detected anomalous CT voxels. Identified anomaly voxel locations  $x_{CT}$ ,  $y_{CT}$ ,  $z_{CT}$  and the corresponding convolution responses  $F_{CT}(x_{CT}, y_{CT}, z_{CT})$  are then stored in the matrices  $A_s$  representing detected high-intensity anomalies and  $A_p$  representing low-intensity anomalies. We find

$$A_s \in \mathbb{R}^{n_s \times 4} \text{ and } A_p \in \mathbb{R}^{n_p \times 4} \quad (5)$$

The respective number of rows  $n_s$  or  $n_p$  represents the number of identified anomalous CT voxels, per type. For this work, all anomalous CT voxels are considered to be undesirable discontinuities.

In contrast to anomalous CT voxels, nominal CT voxels are identified by convolution responses closest to the mean response of the part, as they represent a uniform part density with no interruptions to the typical structure of the material, i.e. *not* a discontinuity. In this work, voxels for which the convolution response falls within  $g_n$  standard deviations of the mean are labeled as nominal, where decreasing the value of  $g_n$  decreases the number of detected nominal CT voxels. Clearly, the values of  $g_a$  and  $g_n$  satisfy  $g_a > g_n$  and are design parameters dictating the search criteria. Similar to the construction of  $A_s$  and  $A_p$ , locations  $x_{CT}$ ,  $y_{CT}$ ,  $z_{CT}$  and convolution responses  $F_{CT}(x_{CT}, y_{CT}, z_{CT})$  of nominal CT voxels are stored in a matrix  $N_n \in \mathbb{R}^{n_n \times 4}$ , where the number of rows  $n_n$  represents the number of identified nominal CT voxels.

## 2.2. Clustering neighboring anomalous CT voxels

Depending on the actual size of the flaw and the resolution of the CT scan data, discontinuities generally consist of multiple anomalous CT voxels. Therefore, clustering adjacent anomalous CT voxels provides a geometrical description of the discontinuity. The proposed clustering method proceeds in two steps and aims to identify discontinuities of a specified minimum size, thereby eliminating anomalous CT voxels below a user-defined cluster size from further analysis.

Step 1: For each anomaly matrix  $A_s$  and  $A_p$ , anomalous CT voxels are removed if they lack  $n_{CT}$  number of neighboring anomalous CT voxels within a pre-defined radius  $d_{CT}$ . This prevent the detection of discontinuities which do not have a volume greater than  $n_{CT}d_{CT}^3$ . The number of anomalous CT voxels is thus reduced from  $n_s$  and  $n_p$  to  $n_{s1}$  and  $n_{p1}$ .

Step 2: In order to exclusively assign each anomalous CT voxel to a specific discontinuity,  $k$ -means clustering [20] is performed. Via  $k$ -means, all remaining anomalous CT voxels are partitioned into  $k$  clusters, and each anomalous CT voxel is assigned to a cluster based on its relative distance to the respective cluster center.

The anomaly matrices  $A_s$  and  $A_p$  can then be amended by one column to include cluster assignments for each anomalous CT voxel. We define  $A_{s1} \in \mathbb{R}^{n_{s1} \times 5}$  and  $A_{p1} \in \mathbb{R}^{n_{p1} \times 5}$ . Again, the added 5th dimension

now indicates an exclusive cluster assignment, where anomalous CT voxels with identical cluster assignments belong to the same discontinuity.

## 2.3. Transferring ground truth labels into *in situ* sensor domains

In order to train a binary classifier for detection of discontinuities in the *in situ* sensor (i.e. the layerwise image) domain, anomalies extracted from CT scan data and contained in  $A_{p1}$ ,  $A_{s1}$ , and  $N_n$  need to be mapped into the *in situ* sensor domain. The required coordinate transformation can be generated from a set of reference points embedded in the part. The respective coordinates of these reference points for either domain, i.e. CT scan or *in situ* sensor, can be extracted either by automation or hand. Based on the two sets of coordinates extracted, an affine mapping function was estimated between the CT scan and *in situ* sensor domains using a least squares approach. The transformation is given by

$$\begin{bmatrix} \hat{x} \\ \hat{y} \\ \hat{z} \end{bmatrix} = A \begin{bmatrix} x_{CT} \\ y_{CT} \\ z_{CT} \end{bmatrix} + B \quad \text{with } A \in \mathbb{R}^{3 \times 3}, B \in \mathbb{R}^{3 \times 1} \quad (6)$$

Here, the coordinates in the CT scan domain are  $x_{CT}$ ,  $y_{CT}$ ,  $z_{CT}$ , and the respective coordinates in the *in situ* sensor domain are  $\hat{x}$ ,  $\hat{y}$ ,  $\hat{z}$ . Residual errors in the coordinate transformation, Eq. (6), can arise due to the non-exact extraction of reference point coordinates. Additionally, distortions in the part, due to thermal deformation, will occur during and after the build. To quantify the accuracy of the transfer of coordinates, the residual root mean square (RMS) error between  $n$  observed domain reference points with coordinates  $(x_{CT}, y_{CT}, z_{CT})$  from the CT scan domain, and  $n$  transformed domain reference points  $(\hat{x}, \hat{y}, \hat{z})$  from *in situ* sensor data can be computed as

$$\begin{aligned} \text{RMS}_x &= \sqrt{\frac{\sum_{i=1}^n (x_{CT,i} - \hat{x}_i)^2}{n}}, \quad \text{RMS}_y = \sqrt{\frac{\sum_{i=1}^n (y_{CT,i} - \hat{y}_i)^2}{n}}, \quad \text{RMS}_z \\ &= \sqrt{\frac{\sum_{i=1}^n (z_{CT,i} - \hat{z}_i)^2}{n}} \end{aligned} \quad (7)$$

## 2.4. Extract features from labeled *in situ* sensor data (i.e. layerwise images)

In order to facilitate machine learning in the *in situ* sensor domain, features are extracted from the *in situ* sensor data, i.e. the layerwise images, for each location for which a ground truth label exists. Feature extraction for voxels within the *in situ* sensor domain, hereafter referred to as DSLR voxels (in reference to the DSLR-based imaging system used in this work), is conducted using 3D convolution filters, similar to the ones described in Section 2.1. Since the melt zone of the laser may extend through several layers, it is deemed critical to assess features through multiple build layers in order to accurately identify discontinuities in the final component. Filter size dimensions can then be defined based on the residual RMS errors from Eq. (7)

$$x_f = \lceil \text{RMS}_x 2 L_s \rceil, \quad y_f = \lceil \text{RMS}_y 2 L_s \rceil, \quad z_f = \lceil \text{RMS}_z 2 L_s \rceil \quad (8)$$

where  $\lceil \cdot \rceil$  denotes the ceiling operation that assigns the least integer greater than or equal to the argument. Here, the parameter  $L_s$  denotes a scaling parameter. Defining the filter size in terms of coordinate transformation RMS error guarantees a predefined level of confidence when transferring the coordinates of labeled discontinuities from the CT scan domain into the *in situ* sensor domain. For example, choosing  $L_s = 2$ , i.e.  $\pm 2$  RMS deviations, implies a 95% confidence (due to errors in the coordinate transformation) that the feature extraction filter of size  $(x_f, y_f, z_f)$  anchored at the estimated discontinuity location will actually encompass the discontinuity in the *in situ* domain.

For a 3D convolution filter of size  $(x_f, y_f, z_f)$  as measured as an integer number of DSLR voxels, there are  $F_n = x_f \cdot y_f \cdot z_f$  linearly independent filters that can be generated, each of which will extract one

particular feature via 3D convolution operation. Extracted features can be placed into a feature matrix of the form

$$M_i \in \mathbb{R}^{n_{total} \times F_n}, i = 1, 2, \dots, V \quad (9)$$

where  $n_{total}$  represents the total number of DSLR voxels, and  $F_n$  represents the total number of extracted features per voxel. In this work, more than one sensor modality is available (i.e. multiple images with different lighting each layer), and so a feature matrix  $M_i$  can be generated for each of the  $V$  individual sensor modalities. Utilizing multiple in situ sensor domains yields multiple observations from which to extract data.

The effectiveness of classification techniques is dependent on having an adequately large sample size, where  $n_{total}$  is greater than the number of features  $F_n$ . In an ideal classification scenario, a one-to-one ratio of anomaly and nominal samples would be available. However, best practices can limit the number of anomalous samples present, i.e. optimized PBFAM processing conditions are expected to generate minimal discontinuities. Attempts to generate an increase in anomalous part behavior by altering processing conditions, e.g. changing hatch spacing, have been shown to create too many discontinuities, thereby limiting the number of nominal samples. Therefore, a one-to-one ratio of nominal to anomalous samples might not be possible in any scenario with binary labels designated as anomalous and nominal, and so more total samples will be required to increase  $n_{total}$  to an acceptable level. There is no mathematical formulism to define how large the sample size must be. However, accurate classification using previously “unseen” test data, i.e. data that was not used for training, coupled with the trained classification model through a cross-validation scheme can provide a good indication of sufficient sample size [21].

### 2.5. Apply the ensemble classification scheme

To fuse information from all feature matrices in Eq. (9) across multiple in situ sensor modalities (i.e. in this case, across multiple images collected for each build layer), an *ensemble* classification scheme [22] is proposed. An ensemble classifier uses a combination of classifier outputs for improved performance, and thus circumvents the high dimensionality (and computational cost) associated with large filters and a large feature space. This is accomplished because each individual classifier operates in a reduced,  $F_n$ -dimensional feature space. Following this strategy, a chosen machine learning method is applied to each feature matrix,  $M_i$ , where the output from each feature matrix for each sample, in terms of decision and associated confidence level, are fed into a second (or master) classifier for final classification. This method creates one model, an *ensemble* of models, using all the information obtained to make a decision in a reduced  $V$ -dimensional feature space with  $n_{total}$  samples, in a feature matrix  $F_E \in \mathbb{R}^{n_{total} \times V}$ . The ensemble classifier thus enables multiple in situ sensor modalities to be utilized in making an assessment of quality. In this work, multiple in situ sensor modalities are realized with multiple images collected under different lighting conditions in each layer. Fig. 3 schematically shows an ensemble classifier fusing the decisions of  $V$  individual classifiers.

## 3. Experiment

### 3.1. Experiment setup and data

A PBFAM build process conducted in an EOS M280 AM system [23] was monitored with an in situ sensor comprising a 36.3-megapixel DSLR camera (Nikon D800E) mounted inside the build chamber. Using combinations of five light sources to generate a total of eight different lighting conditions, the DSLR camera captured multiple images each build layer. The experimental setup is shown in Fig. 4. The various lighting sources added to the system, designated as *flash modules*, were covered with several layers of light-diffusing film. Timing of image capture was triggered via proximity-sensor monitoring of the recoater

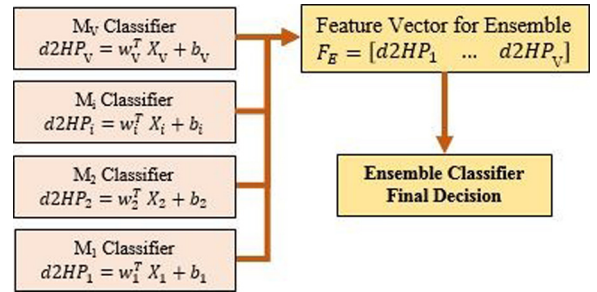


Fig. 3. Ensemble classification scheme, merging  $V$  individual classifiers.

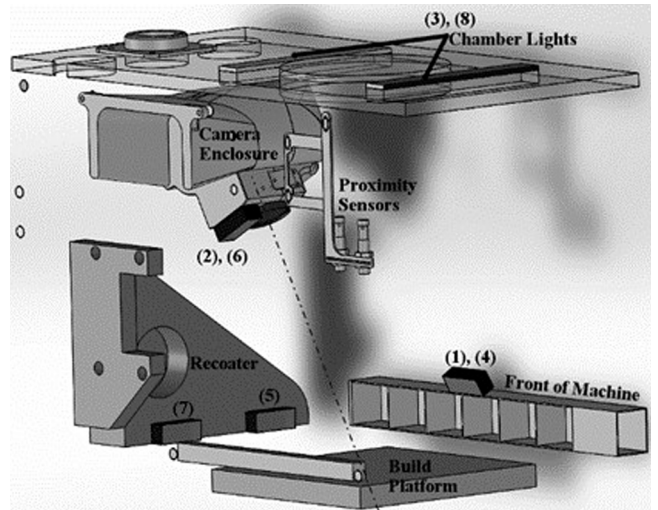


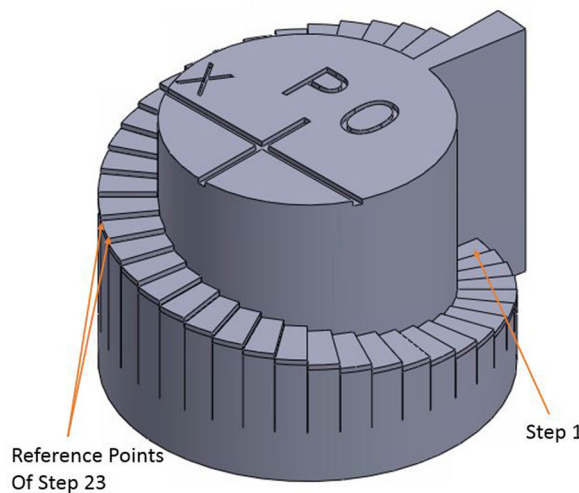
Fig. 4. Location of camera system and light sources in the build chamber. Eight individual flash configurations (or flash modules) are used with sequence (1)–(8).

blade, with images (1)–(3) captured immediately following the powder recoating operation, and images (4)–(8) collected immediately following the laser fusion step. Additional details concerning the camera and light systems are reported in Ref. [24].

For this investigation, a single stainless steel part, denoted as a *step cylinder*, was built with EOS Stainless Steel GP-1 powder using the EOS standard exposure parameters and processing strategy for 20  $\mu\text{m}$  layers. The 10 mm tall  $\times$   $\varnothing$  10 mm cylinder with an encircling 39 step staircase, and step height of 200  $\mu\text{m}$  (10 layers), is displayed in Fig. 5. The small size of the test part allows for high resolution in the post-build CT scans. The 39 step staircase was incorporated into the design to provide 78 unique reference points (i.e. both free corners of each step) from which a coordinate transformation between the in situ sensor domain and CT scan domain could be estimated. The resulting coordinate transformation accounts for part misalignments in both domains, as well as thermally induced distortion that occurs during the build and after removal of the test part from the build plate.

The in situ sensor data (eight images per build layer), were cropped to the step cylinder. Grayscale representations of the DSLR images were stacked to create multiple 3D representations of the build process, one for each of the eight images captured from each layer. DSLR voxels in the in situ sensor domain are defined by image resolution and build layer height ( $\sim 50\text{-}\mu\text{m}/\text{pixel}$  xy image resolution, 20  $\mu\text{m}/\text{layer}$ ) in each image stack<sup>1</sup>. Then, the grayscale intensity  $I_f(x_i, y_i, z_i, f_i) \in \mathbb{R}$  is a function of the voxel location  $x_i, y_i, z_i$  (representing the row, column, and layer), as well as the image index  $f_i \in \{1, 2, \dots, 8\}$  (representing the

<sup>1</sup> Note that xy resolution provided is an approximation, since the parallax distortion resulting from off-axis imaging leads to varying resolution across the image frame.



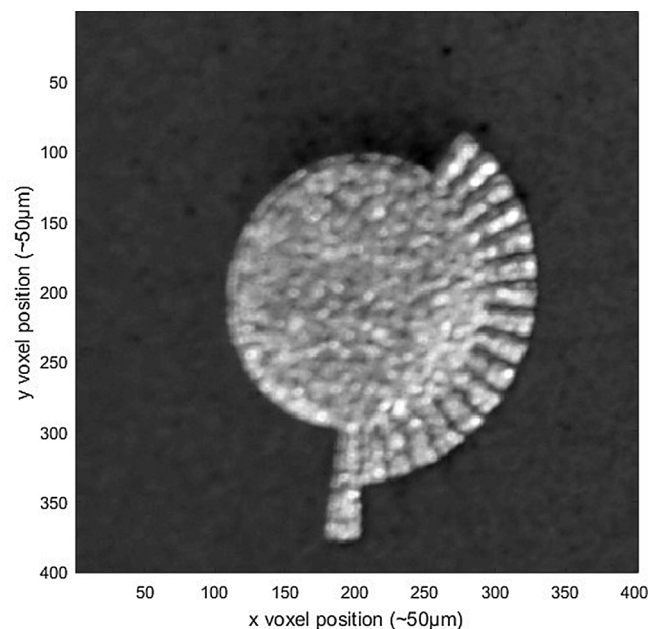
**Fig. 5.** 3D CAD model of step cylinder including 78 reference points, two for each of the 39 steps.

image corresponding to each individual flash module). For the data used in this study the dimensions of the  $I_f$  domain are [400, 400, 555, 8]. Fig. 6 displays the eight images, one for each flash module, taken from one layer. Fig. 7 displays an enlarged image from flash module  $f = 6$ , i.e. post-fusion.

In addition to layerwise imagery, part contour coordinates for each build layer were extracted from the EOS M280 system slice files. Slicing data, hereafter denoted as the SLI domain, for the 23rd step on the staircase is shown in Fig. 8.

Post-build CT scans were obtained from the part after removal from the build plate. Fig. 9 displays a CT image layer, specifically the gray scale intensity of Eq. (1), also corresponding to the 23rd step on the staircase. The CT scan domain is discretized into 15  $\mu\text{m}$  cubic voxels, yielding CT scan domain dimensions of [1009, 1103, 715].

For this investigation, the EOS M280 system settings were set to EOS standard conditions, which were expected to result in a minimal number of anomalies (i.e. discontinuities), and an abundant number of nominal (i.e. fully dense) conditions. This approach for the AM system



**Fig. 7.** Large image of flash module 6, post-fusion, image from step 23.

settings was used to create a part with relatively few, isolated discontinuities, which could be easily compared to nominal sections of the part using CT scan data. Hatch distance was 0.1 mm, scan speed was 1000 mm/s, layer thickness 20  $\mu\text{m}$ , and laser power was 195 W. To eliminate complexities of discontinuity classification near edges of complex geometries, only anomalies in the central cylindrical region of the step cylinder were used for discontinuity detection during analysis. This approach was implemented through masking, so that the complex geometries of the staircases could not interfere or skew the classification of discontinuities via machine learning.

### 3.2. Coordinate transformation

A coordinate transformation was generated between in situ sensor and CT scan domains using a least squares approach that matches the

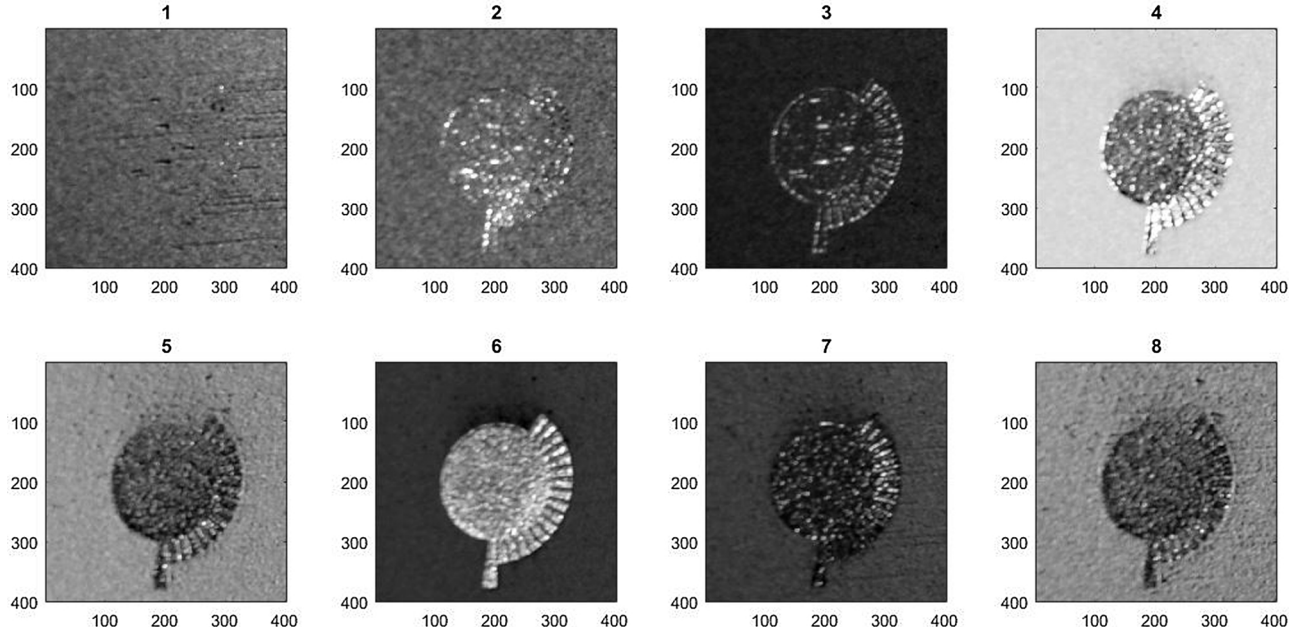


**Fig. 6.** In situ sensor imagery, i.e. eight flash module images taken at step 23: (1)–(3) post powder recoating flash modules and (4)–(8) post fusion flash modules.

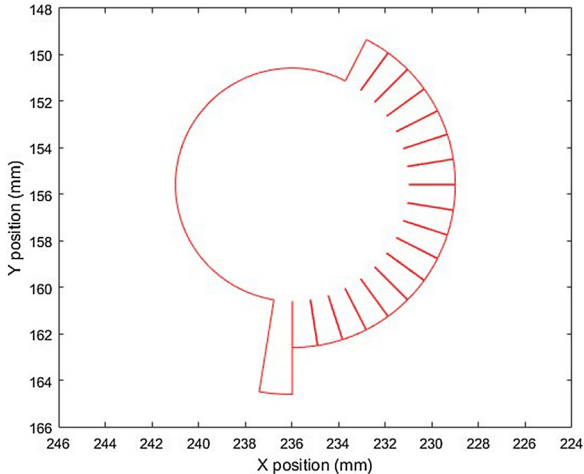


**Fig. 8.** Slicing data image of step 23 extracted from EOS M280 system slice files and showing part contour.

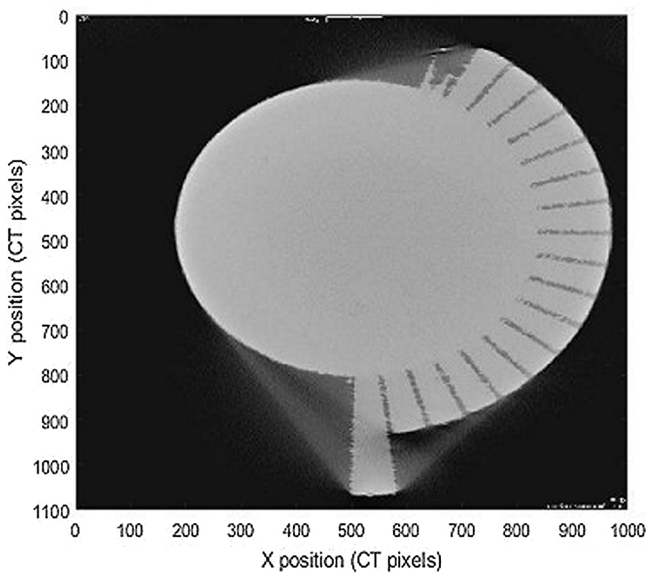


**Fig. 9.** CT scan image, specifically gray scale intensity  $I_{CT}$  form (1), approximately corresponding to layer of step 23.

78 reference points provided by the staircase. The corresponding affine transformation (Eq. (6)) then captures rotation, linear distortion, and translation. To aid in formulating this transformation, the coordinates of each individual slice, generated by the AM software from the original CAD model, are stored in the SLI domain. In this case, reference points in all domains (in situ sensor, CT scan, and SLI) were hand-labeled. To improve the accuracy of the coordinate transformation, which is degraded by the locational uncertainty introduced during extraction of reference points in the in situ sensor and CT scan domains, the SLI domain was used as an interim domain, i.e. both in situ sensor and CT scan data were mapped to the SLI domain prior to being mapped to each other. Assuming a well-calibrated laser scanner, no offsets of laser contours, and perfect galvanometer calibration, the SLI domain coordinates may act as a ground truth, representative of the actual EOS M280 laser path.

### 3.3. Filter design and feature extraction

Filter dimensions of Eq. (8) were set equal to two RMS errors, i.e.  $L_s = 2$ , for length, width and height. Additionally, the filter size was increased to be made square in the xy-plane.

Given the filter size  $(x_f, y_f, z_f)$  with  $x_f, y_f$ , and  $z_f$ , representing an integer number of DSLR voxels,  $F_n = x_f \cdot y_f \cdot z_f$  linearly-independent filters can be created, where one filter extracts one feature, i.e. one column in the feature matrix  $M_i$  in Eq. (9). This is done by setting only one filter element to 1 at a time, while the remaining  $F_n - 1$  elements in a filter are set to zero. In this manner, any additional filter constructed would be a linear combination of the first  $F_n$  filters, and thus contain no additional information for subsequent linear classification.

### 3.4. CT labels and clustering

Gaussian convolution responses from the CT scan domain were generated with varying kernel sizes,  $S = [3, 5, 7, 9, 11]$  voxels ( $(15 \mu\text{m})^3/\text{voxel}$ ), from Eqs. (2) and (3). The selected kernel sizes mimic diameters of anticipated discontinuities, typically between  $15 \mu\text{m}$  and  $200 \mu\text{m}$  [19]. A mask was applied to the CT scan domain to limit the generation of convolution responses to the center cylindrical region of the step cylinder, thereby excluding the edge of the part, staircase, and background.

Anomaly matrices,  $A_s$  and  $A_p$  from Eq. (5), were filled with CT voxel locations whose convolution response for CT anomaly detection from Eq. (4) fell outside  $g_a = 4$  standard deviations from the mean of the part, roughly 0.006% of the entire data set for any selected kernel size  $S$  in Eq. (3). Anomalous CT voxels were clustered as outlined in Section 2.2, while clusters containing fewer than three (3) CT voxels and clusters with a diameter of less than  $20 \mu\text{m}$  were discarded from further analysis.

Nominal voxels were identified if the convolution response for CT anomaly detection from Eq. (4) fell within  $g_n = 1$  standard deviation of the mean of the entire part and were not within a neighborhood of the anomalous CT voxel bounded by the distance in the CT domain corresponding to the filter extraction distance in the in situ sensor domain. This range specification prevented feature extraction overlap between anomaly voxels and nominal voxels during subsequent SVM classification.

Furthermore, once selected, ground truth labels were manually confirmed by an inspector with ANST NDT Level III certification in Radiographic Testing to ensure sufficient data quality.

### 3.5. Sample size versus feature dimension

The decrease in resolution between the CT scan domain and in situ sensor domain results in a reduction of samples (or data points) in the in situ sensor domain, i.e. multiple CT voxels may get mapped to the same DSLR voxel. To ensure that the sample size,  $n_{total}$  is greater than the number of extracted features  $F_n$ , both defined as number of rows and columns of  $M_i$  in Eq. (9), the ratio of anomalous samples to nominal samples can be altered. Assuming that the number of anomalous samples will be low, the number of nominal samples present in each feature matrix was increased to meet a defined requirement that total samples be at least four times greater than the number of features for any training data set during four-fold cross validation.

### 3.6. Cross-validation of a linear SVM classification and ensemble classification scheme

In this work, linear Support Vector Machines (SVMs) [17] were chosen as binary classifiers to detect flaws in the in situ sensor data using features extracted from the layerwise images, contained as rows in  $M_i$  in Eq. (9). Use of a simple, non-parametric model enables weighting of different inputs associated with the various images collected each layer and the corresponding extracted feature dimensions. Additionally, the ensemble classification scheme from Fig. 3 can easily be extended to include data from additional sensors if desired. From [17], linear SVMs generate a maximum margin separating hyperplane in a  $F_n$ -dimensional feature space where  $w_i \in \mathbb{R}^{F_n}$  is the normal vector

of the hyperplane and  $b_i \in \mathbb{R}$  is the bias. Then, the hyperplane is defined by

$$h_i(\bar{x}) = w_i^T \bar{x} + b_i = 0 \text{ with } \bar{x} \in \mathbb{R}^{F_n} \quad (10)$$

Classification is determined by a feature vector's location relative to the hyperplane, which can be computed as decision value or signed distance function

$$d_i(\bar{x}) = w_i^T \bar{x} + b_i \in \mathbb{R} \quad (11)$$

taking a positive value on one side of the hyperplane and negative on the other [25].

Four-fold cross-validation was implemented to validate the effectiveness of the linear SVM classification method. Four-fold cross-validation divides the data into four subsets, using equalized random sampling (each subset was selected to contain an equal number of nominal and anomalous samples). Each subset was tested with a model generated by the remaining three subsets acting as training data. This was repeated for each subset. Validation of sufficient samples size and effectiveness of linear SVM classification can be shown by demonstrating similar model performance for each of the individual folds.

Given the ensemble classification scheme, each feature matrix  $M_i$ ,  $i = 1, 2, \dots, V$  in Eq. (9), i.e. one for each of the eight flash modules, underwent linear SVM classification, creating  $V = 8$  distinct SVM models. As shown in Fig. 3, outputs of the first state of linear SVM classifiers were fed into another linear SVM classifier in the form of the decision value  $d_i(\bar{x})$  from Eq. (11) in order to create a second-stage SVM model, i.e. the ensemble classifier. Test data, i.e. data not previously used for training, was then fed through both stages, so that the resulting out-of-sample classification performance could be assessed.

Validation of linear SVM classification performance was formally analyzed via a confusion matrix using accuracy, recall and precision of each testing data subset, defined below

$$\begin{aligned} \text{Accuracy} &= \frac{\sum (\text{True positive} + \text{True Negative})}{\sum \text{Total Population}} \\ \text{Recall} &= \frac{\sum \text{True positive}}{\sum (\text{True Positive} + \text{False Negative})} \\ \text{Precision} &= \frac{\sum \text{True positive}}{\sum (\text{True Positive} + \text{False Positive})} \end{aligned} \quad (12)$$

Here, true positives are anomalous samples (corresponding to regions labeled as discontinuities in the CT data), that were *properly* classified as anomalous samples using the in situ sensor data, alone. True negatives are nominal samples that were *properly* classified as nominal samples. The performance of SVM classification was evaluated using two methods: (i) discrimination of *individual* DSLR voxels between anomaly and nominal with no regard to cluster assignments, and (ii) evaluating discontinuity cluster detection whereby an *entire discontinuity cluster* is assumed to be detected if a single DSLR voxel was determined to be a discontinuity. The former represents a machine learning standard for rigorous classification performance, while the latter mimics a methodology more meaningful in an industrial setting where discontinuity mitigation is sought. When implemented in an AM process monitoring and control system, an identified anomalous DSLR voxel could trigger corrective action, e.g. re-melting of the local region to repair the discontinuity, before the next layer is processed.

## 4. Results

### 4.1. Coordinate transformation and filter dimensions

The transformation of reference points from the CT scan domain into the in situ sensor domain is displayed in Fig. 10. The calculated RMS errors from Eq. (7) were  $\sim 1.75$ ,  $\sim 1.5$ , and  $\sim 0.75$  DSLR voxels in the x, y, and z directions, corresponding to  $87.5$ ,  $75$ , and  $37.5 \mu\text{m}$ . Based

on these RMS errors and the discussion in Section 2.4, a filter size of  $7 \times 7 \times 3$  DSLR voxels was chosen for feature extraction in the in situ sensor domain, yielding  $F_n = 7 \times 7 \times 3 = 147$  linearly independent filters.

### 4.2. Anomaly labels in the CT scan and in situ sensor domains

As noted earlier, clusters of labeled anomalies that were identified in the CT scan domain were manually evaluated and validated to be flaws by an inspector with ANST NDT Level III certification in Radiographic Testing in order to ensure correct ground truth labeling. Inspection revealed no high-intensity CT voxels for this data set, i.e. no identified inclusions, and so the matrix  $A_s$  in Eq. (5) was empty for this experiment. However,  $n_p = 497$  low-intensity, anomalous CT voxels, likely belonging to incomplete fusion or porosity, were identified in CT scan data, of which  $n_{p1} = 456$  CT voxels could be partitioned into a total 38 clusters (believed to correspond to 38 individual flaws) using k-means clustering [20]. Fig. 11 displays a cluster that was automatically detected in the CT scan domain (and manually verified to be a discontinuity), which consists of tens of individual CT voxels and extends through multiple layers of the CT scan. Each layer in Fig. 11 is centered on the centroid of the cluster, with image dimensions set to  $80 \times 80$  CT pixels ( $1200 \times 1200 \mu\text{m}$ ).

The coordinates of the cluster depicted in Fig. 11 were transferred from the CT scan domain into the SLI domain and then into the in situ sensor domain using the coordinate transformations in Eq. (6). Fig. 12 displays the corresponding four layers in the flash module 6 images centered at the centroid of the discontinuity. The red box is provided as a physical representation of the size of the feature extraction filter ( $7 \times 7 \times 3$  DSLR voxels) in the in situ sensor domain, i.e. the neighborhood from which visual features will be extracted for latter classification.

For performance evaluation, clusters were divided into five classes based on the number of CT voxels in each cluster [4–7, 8–11, 12–15, 16–19,  $> 20$ ], corresponding to the volume of each cluster, [ $13.5$ – $23.6$ ,  $27$ – $37.1$ ,  $40.5$ – $50.6$ ,  $54.0$ – $64.1$ ,  $> 67.5 \times 10^3 \mu\text{m}^3$ ], and the diameter of a spherical discontinuity that would have equivalent volume [29.5–35.6, 37.2–41.4, 42.6–45.9, 46.9–49.7,  $> 50.5 \mu\text{m}$ ]. The frequency (or number of occurrences) of each cluster size class, and the total number of voxels per class in the CT scan domain, are displayed in Fig. 13 in blue and green, respectively. As an example, the data reveal that there were only 4 clusters in the CT scan domain that correspond to a discontinuity with diameter  $> 50.5 \mu\text{m}$ .

Transferring coordinates from the high-resolution CT scan domain to the lower resolution in situ sensor domain reduced the total number of data points from 456 CT voxels to 168 DSLR voxels. In contrast to Figs. 13, 14 now displays the frequency of each cluster size in the in situ sensor domain, as well as the total number of DSLR voxels per class. DSLR cluster size definition for the five classes now corresponds to [1, 2, 3, 4,  $> 5$ ] DSLR voxels.

### 4.3. Feature matrices

For Eq. (9), sample size  $n_{total}$  was dictated by the requirement for more samples than features extracted  $F_n = 147$ , which is defined by the filter size. Therefore, each feature matrix  $M_i$  was assigned a total number of  $n_{total} = 840$  samples, made up of the 168 identified discontinuity DSLR voxels and 672 additional nominal DSRL voxels, so that  $n_{total} > 4F_n$  satisfies the criteria established in Section 3.5. Those additional 672 nominal DSRL voxels were randomly chosen from the 1,600 nominal DSLR voxels identified.

### 4.4. Classification results

Classification results for accuracy, recall and precision from Eq. (12) are displayed in Table 1, defined in terms of average value  $\pm$  one standard deviation cumulated over the four-fold cross-validation

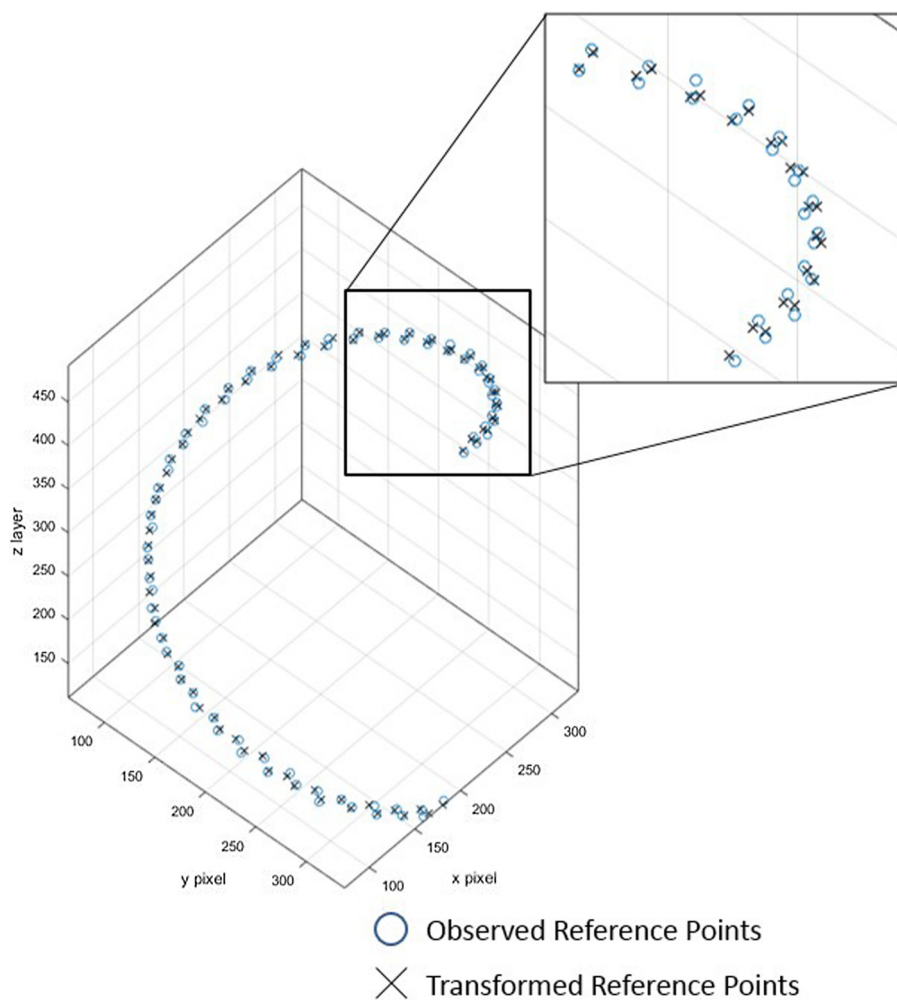


**Fig. 10.** Transformed reference points from CT scan domain into the in situ sensor domain using estimated affine transformation (6).

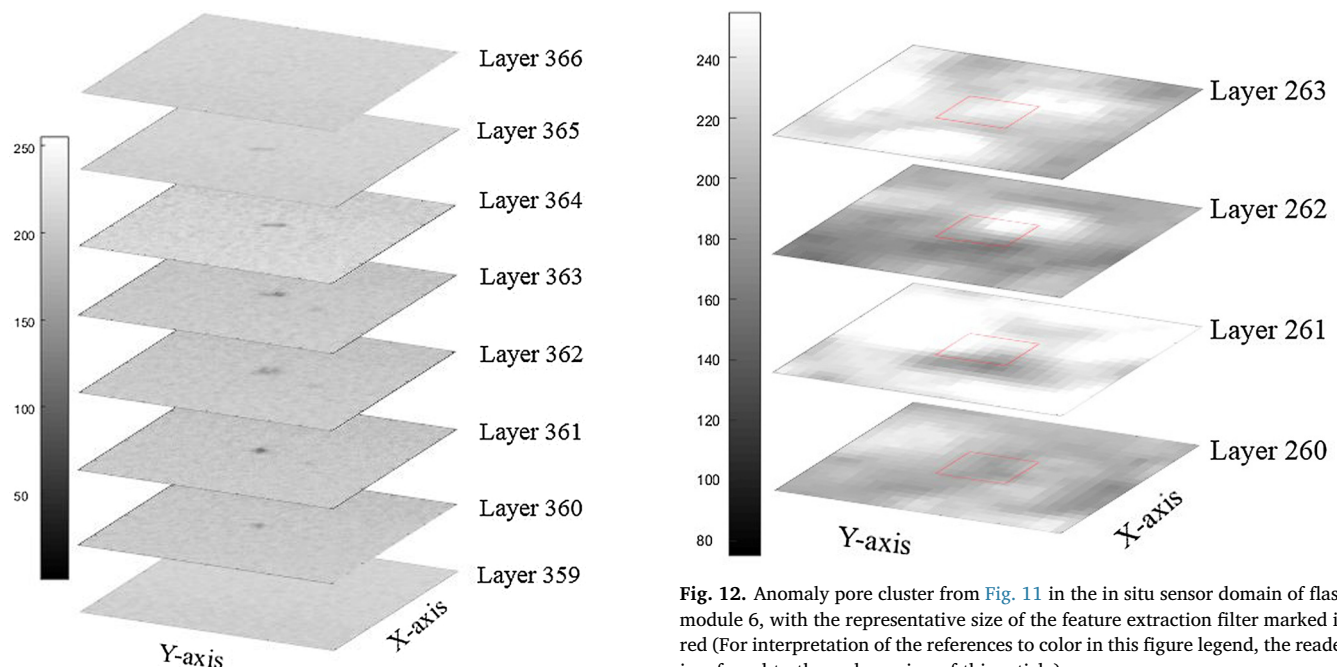


**Fig. 11.** CT image layers 359 to 366 containing an anomaly pore cluster detected comprising of 36 CT voxels from layers 360 to 364 in the CT scan domain.

**Fig. 12.** Anomaly pore cluster from Fig. 11 in the in situ sensor domain of flash module 6, with the representative size of the feature extraction filter marked in red (For interpretation of the references to color in this figure legend, the reader is referred to the web version of this article).

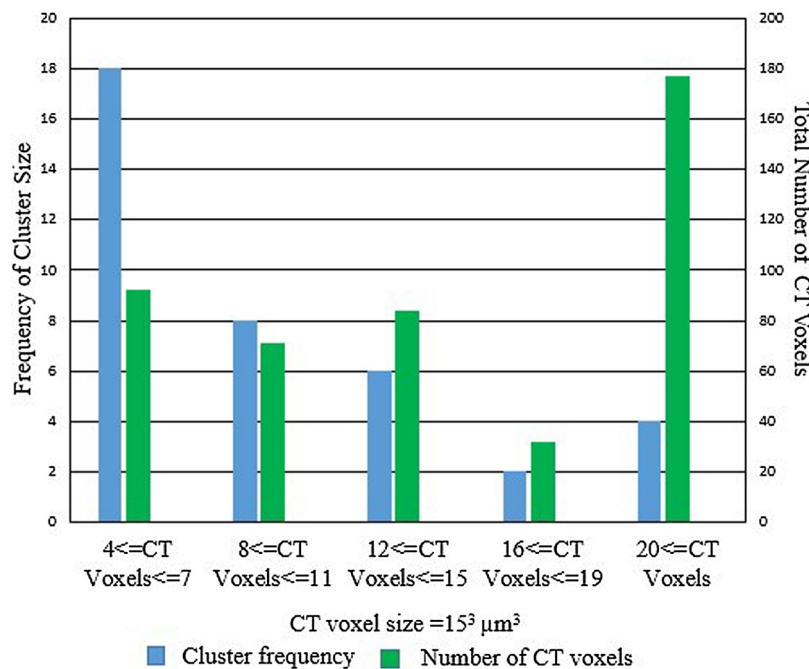


**Fig. 13.** Frequency of CT cluster class size (blue) and total number of CT voxels per class (green) (For interpretation of the references to color in this figure legend, the reader is referred to the web version of this article).

models. Again, one cross-validation model corresponds to a specific choice for data partitioning into training and test data. The results are shown for each individual feature matrix SVM classifier and for the ensemble SVM classifier. Accuracies for the classifiers in Table 1 are all well above 50%, demonstrating the ability to discriminate discontinuities in layerwise DSLR images both individually and in an ensemble scheme. Similar performance for all cross-validation models, represented by the small standard deviation, confirms sufficient sample size and consistency between SVM classifiers. The ensemble classifier, that fuses information from all eight flash modules as shown in Fig. 3, achieved ~85% accuracy compared to the individual flash module classifiers ranging from 63%–73%, thus confirming that inclusion of

data from all modalities, i.e. all flash modules, improves accuracy.

Fig. 15 displays the total number of DSLR voxels per cluster size class (in blue) along with the total number of true positive classification of DSLR voxels for each cluster size class (green). The latter is representative of the recall metric shown in Table 1. Fig. 15 is representative of the standard evaluation for machine learning models, and illustrates that an increase of discontinuity size correlates to an increase in detection performance. It is evident that recall improves for larger discontinuities.

However, in a practical application such as PBFAM process monitoring, it is not necessary to identify every DSLR voxel that corresponds to a discontinuity comprising multiple CT voxels. If a single DSLR voxel

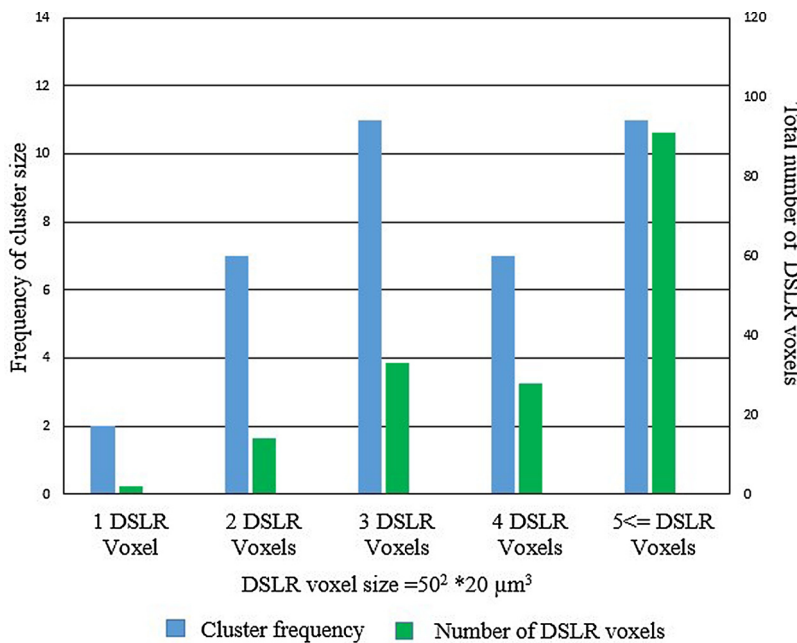


**Fig. 14.** Frequency of cluster size class (blue) and total number of DSLR voxels (green) in the in situ sensor domain per class (For interpretation of the references to color in this figure legend, the reader is referred to the web version of this article).

**Table 1**

Average value and standard deviations of accuracy, precision and recall for each feature matrix SVM classifier and ensemble classifier.

Feature matrix of flash model	Accuracy $\pm$ 1 Std. Dev.	Precision $\pm$ 1 Std. Dev.	Recall $\pm$ 1 Std. Dev.
1	0.72 $\pm$ 0.012	0.37 $\pm$ 0.015	0.42 $\pm$ 0.049
2	0.62 $\pm$ 0.023	0.24 $\pm$ 0.051	0.53 $\pm$ 0.121
3	0.71 $\pm$ 0.034	0.35 $\pm$ 0.044	0.55 $\pm$ 0.023
4	0.66 $\pm$ 0.042	0.31 $\pm$ 0.049	0.55 $\pm$ 0.105
5	0.63 $\pm$ 0.058	0.27 $\pm$ 0.052	0.51 $\pm$ 0.100
6	0.73 $\pm$ 0.042	0.39 $\pm$ 0.047	0.63 $\pm$ 0.083
7	0.64 $\pm$ 0.049	0.29 $\pm$ 0.042	0.54 $\pm$ 0.023
8	0.68 $\pm$ 0.008	0.33 $\pm$ 0.022	0.60 $\pm$ 0.079
Ensemble Classifier	0.85 $\pm$ 0.015	0.64 $\pm$ 0.029	0.60 $\pm$ 0.049

is identified as discontinuity, a corrective action, such as re-melting, can be triggered for the local region. Fig. 16 displays the frequency of each cluster size class in the DSLR domain along with total number of successfully detected discontinuity clusters of that size in the CT scan domain. All but one cluster (i.e. 17 out of 18) was accurately identified for clusters with  $> 4$  DSLR voxels, roughly corresponding to a flaws with equivalent diameter  $> 47 \mu\text{m}$ .

## 5. Conclusion

Effectiveness of the ensemble classifier scheme, including the confirmation of a sufficient sample size, was validated by the similar performance of classification between each cross-validation model. The relative high performance of the classification ensemble demonstrated the potential to discriminate between anomalous and nominal DSLR voxels using in situ sensor modality comprising layerwise imaging collected by a DSLR camera. Implementation of an ensemble classification scheme, paired with a non-parametric machine learning model, enabled the use of high dimensional feature vectors in concert with a relatively small number of sample vectors.

The improvement from 65% accuracy using individual flash modules to 85% accuracy using the ensemble classifier demonstrated that classification performance improves with increasing sensor information. Therefore, in order to make an informed decision on part quality, multiple images, collected under different lighting conditions, should be used. Using an ensemble classification scheme created a framework

for online process monitoring which can easily be extended to include other in situ sensor modalities, such as additional cameras and flash modules. Using reference points to create coordinate transformations for ground truth labels enables the incorporation of data from additional position-synchronized sensors into the ensemble classifier, acting as a system independent approach for sensor validation.

Enabling discontinuities to be identified by detecting a single anomalous DSLR voxel, is an effective technique to increase the accuracy of discontinuity detection, as demonstrated in Fig. 16. With a majority of anomaly clusters extracted being larger than 2 DSLR voxels, single voxel detection is a valid means to detect discontinuities. This discontinuity detection methodology is well suited for in situ layerwise discontinuity mitigation in an industrial setting, providing accurate information related to part quality from DSLR voxel information alone.

In situ layerwise imaging is a system-independent process monitoring technique which can be suited to a range of PBFAM systems. Paired with machine learning, in situ layerwise imaging can be an implemented inexpensively and easily integrated with other monitoring systems or sensor modalities. Improvements on the experiment include increasing image resolution, improving machine vision lighting, adding additional cameras (perhaps to include thermal imaging cameras), adding additional sensor modalities, removing the reliance on embedded reference points for calibration of coordinate transformations, and testing the ability to detect near edges of parts and in complex geometries.

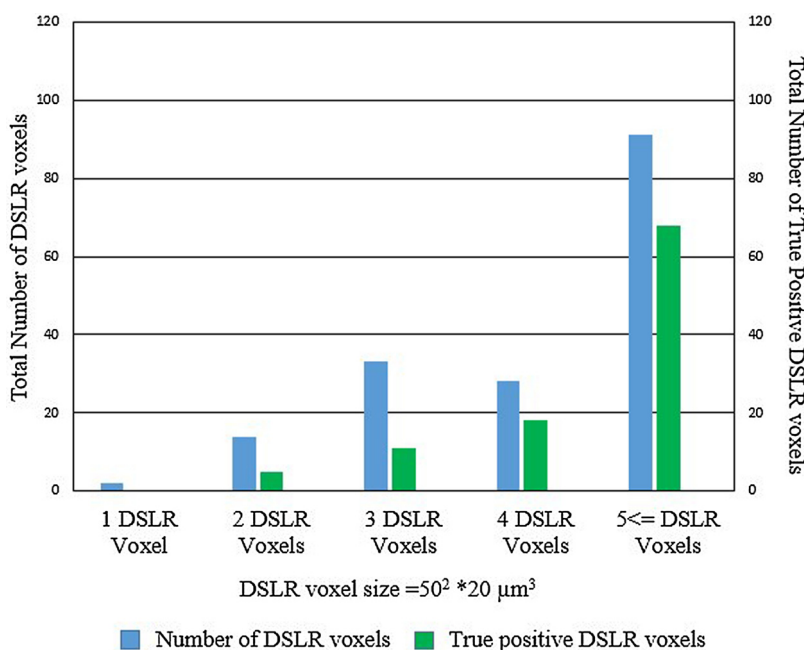
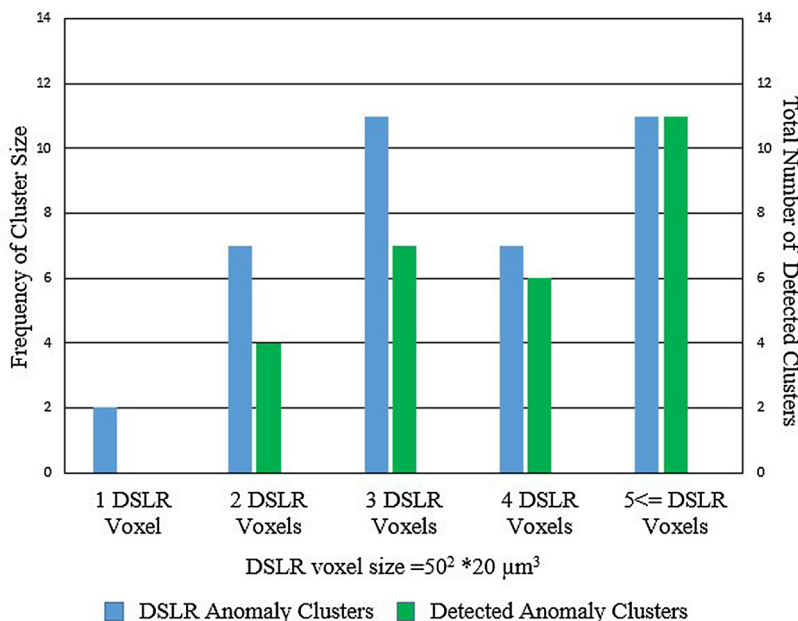


Fig. 15. Total number of DSLR voxels (blue) and true positives DSLR voxels (green) for each cluster size class (For interpretation of the references to color in this figure legend, the reader is referred to the web version of this article).



**Fig. 16.** Frequency of cluster size (blue) and detected clusters (green) per cluster size in the in situ sensor domain based on the number of DSLR voxels (For interpretation of the references to color in this figure legend, the reader is referred to the web version of this article).

## Acknowledgements

This work would not have been possible without the contributions of several individuals. We would like to thank Penn State College of Engineering for supporting Christian Gobert during this project. We would like to thank Naval Air Systems Command for their support. We would also like to thank Ms. Gabrielle Gunderman and Mr. Griffin Jones, from ARL Penn State for their efforts designing the experiments and for performing post-process inspection via 3D computed tomography analysis. Finally, we wish to thank Mr. Don Natale, Mr. Jacob Morgan, and Mr. John Morgan for their contributions in the area of imaging system design and calibration, and for their thoughts on design of the test artifact.

This material is based upon work supported by the Naval Air Systems Command (NAVAIR) under Contract No. N00024-12-D-6404, Delivery Order 0321. Any opinions, findings and conclusions or recommendations expressed in this material are those of the authors and do not necessarily reflect the views of the Naval Air Systems Command (NAVAIR).

## References

- [1] ASTM Standard, ASTM International, Standard Terminology for Additive Manufacturing-General Principles-Terminology, ASTM F42 Committee, (2015).
- [2] W. Gao, Y. Zhang, D. Ramanujan, K. Ramani, Y. Chen, C. Wang, Y. Shen, S. Zhang, P. Zavattieri, The status, challenges, and future of additive manufacturing in engineering, *Comput.-Aided Des.* 69 (2016) 65–89.
- [3] W.J. Sames, F.A. List, S. Pannala, R.R. Dehoff, S.S. Babu, The metallurgy and processing science of metal additive manufacturing, *Int. Mater. Rev.* (2016) 2016–2063.
- [4] H. Gong, K. Rafi, H. Gu, G. Ram, T. Starr, B. Stucker, Influence of defects on mechanical properties of Ti-6Al-4V components produced by selective laser melting and electron beam melting, *Mater. Des.* 86 (2015) 545–554.
- [5] S. Yavari, S. Ahmadi, R. Wauthle, B. Pouran, J. Schrooten, H. Weinans, A. Zadpoor, Relationship between unit cell type and porosity and the fatigue behavior of selective laser melted meta-biomaterials, *J. Mech. Behav. Biomed. Mater.* 43 (2015) 91–100.
- [6] Q.C. Liu, J. Elambasseril, S. Sun, M. Leary, M. Brandt, P.K. Sharp, The effect of manufacturing defects on the fatigue behavior of Ti-6Al-4V specimens fabricated using selective laser melting, *Adv. Mater. Res.* 891–892 (2014) 1519–1524.
- [7] G. Tapia, A. Elwany, A review on process monitoring and control in metal-based additive manufacturing, *J. Manuf. Sci. Eng.* 136 (6) (2014) 60801–60811.
- [8] W. Frazier, Metal additive manufacturing: a review, *J. Mater. Eng. Perform.* 23 (6) (2014) 1917–1928.
- [9] S. Kleszczynski, J. zur Jacobsmühlen, J. Sehrt, G. Witt, Austin, TX, Error Detection in Laser Beam Melting Systems by High Resolution Imaging, 23rd International Solid Freeform Fabrication Symposium (2012).
- [10] J. zur Jacobsmühlen, S. Kleszczynski, D. Schneider, G. Witt, Minneapolis, MN, High Resolution Imaging for Inspection of Laser Beam Melting Systems, IEEE International Instrumentation and Measurement Technology Conference (2013).
- [11] J. Mireles, S. Ridwan, P. Morton, A. Hinojosa, R. Wicker, Analysis and correction of defects within parts fabricated using powder bed fusion technology, *Surf. Topogr. Metrol. Prop.* 3 (2015).
- [12] J. Schwerdtfeger, R.F. Singer, C. Körner, In situ flaw detection by IR-imaging during electron beam melting, *Rapid Prototyp. J.* 18 (4) (2012) 259–263.
- [13] A.B. Spierings, M. Schneider, R. Eggensberger, Comparison of density measure techniques for additive manufactured metallic parts, *Rapid Prototyp. J.* 17 (2011) 380–386.
- [14] W.W. Wits, S. Carmignato, F. Zanini, T.H.J. Vaneker, Porosity testing methods for the quality assessment of selective laser melted parts, *CIRP Ann. Manuf. Technol.* 65 (2016) 201–204.
- [15] A. Weckenmann, X. Jiang, K.-D. Sommer, U. Neushaefer-Rube, J. Seewig, L. Shaw, et al., Multisensor data fusion in dimensional metrology, *CIRP Ann. Manuf. Technol.* 58 (1) (2009) 701–721.
- [16] M. Aminzadeh, T. Kurfess, Layerwise automated visual inspection in laser powder-bed additive manufacturing, AMSE 2015 International Manufacturing Science and Engineering Conference, Charlotte, NC, 2015.
- [17] C. Cortes, V. Vapnik, Support-vector networks, *Mach. Learn.* 20 (3) (1995) 273–297.
- [18] Collaboration for Nondestructive Testing, Radiograph Interpretation – Welds, Nondestructive Testing (NDT) Resource Center, Education Resources, 2007, <https://www.nde-ed.org>.
- [19] S. Evertson, M. Hirsch, P. Stravroulakis, R. Leach, A. Clare, Review of in-situ process monitoring and in-situ metrology for metal additive manufacturing, *Mater. Des.* 95 (2016) 431–445.
- [20] A. Jain, Data ClusteringL 50 years beyond k-means, *Pattern Recognit. Lett.* 31 (2010) 651–666.
- [21] P. Matvkiewicz, J. Pestian, Effect of small sample size on text categorization with support vector machines, Proceedings of the 2012 Workshop on Biomedical Natural Language Processing, Montreal, Canada, 2012.
- [22] B. Waske, J. Benediktsson, Fusion of support vector machines for classification of multisensor data, *IEEE Trans. Geosci. Remote Sens.* 45 (2007) 3858–3866.
- [23] EOSINT M 280. [http://www.eos.info/systems\\_solutions/metal/systems\\_equipment/eosint\\_m280](http://www.eos.info/systems_solutions/metal/systems_equipment/eosint_m280) (Accessed 13 August 2016).
- [24] B.K. Foster, E.W. Reutzel, A.R. Nassar, B.T. Hall, S.W. Brown, C.J. Dickman, Optical layerwise monitoring of powder bed fusion, Solid Freeform Fabrication Symposium Proceedings, Austin, TX, 2015.
- [25] T. Howley, M. Madden, The genetic kernel support vector machine: description and evaluation, *Artif. Intell. Rev.* 24 (2005) 379–395.